



Clarke, H., Verdon, J. P., Kettleby, T., Baird, A. F., & Kendall, J-M. (2019). Real time imaging, forecasting and management of human-induced seismicity at Preston New Road, Lancashire, England. *Seismological Research Letters*, 90(5), 1902-1915. <https://doi.org/10.1785/0220190110>

Peer reviewed version

Link to published version (if available):  
[10.1785/0220190110](https://doi.org/10.1785/0220190110)

[Link to publication record in Explore Bristol Research](#)  
PDF-document

This is the author accepted manuscript (AAM). The final published version (version of record) is available online via Seismological Society of America at <https://pubs.geoscienceworld.org/ssa/srl/article-abstract/572863/real-time-imaging-forecasting-and-management-of?redirectedFrom=fulltext>. Please refer to any applicable terms of use of the publisher.

## University of Bristol - Explore Bristol Research

### General rights

This document is made available in accordance with publisher policies. Please cite only the published version using the reference above. Full terms of use are available: <http://www.bristol.ac.uk/red/research-policy/pure/user-guides/ebr-terms/>

1 **Real time imaging, forecasting and management of**  
2 **human-induced seismicity at Preston New Road,**  
3 **Lancashire, England**

4 Authors: Huw Clarke<sup>1</sup>, James P. Verdon<sup>2</sup>, Tom Kettlety<sup>2</sup>, Alan F. Baird<sup>2</sup>,  
5 J-Michael Kendall<sup>2</sup>

6

7 *1. Cuadrilla Resources Ltd., Cuadrilla House, 6 Sceptre Court, Bamber Bridge,*  
8 *Lancashire, U.K., PR5 6AW.*

9 *2. School of Earth Sciences, University of Bristol, Wills Memorial Building, Queen's*  
10 *Road, Bristol, U.K., BS8 1RJ.*

11

12

13

14

## ABSTRACT

15

16 *Earthquakes induced by subsurface fluid injection pose a significant issue across a range of industries.*  
17 *Debate continues as to the most effective methods to mitigate the resulting seismic hazard.*  
18 *Observations of induced seismicity indicate that the rate of seismicity scales with the injection volume,*  
19 *and that events follow the Gutenberg-Richter distribution. These two inferences permit us to populate*  
20 *statistical models of the seismicity, and extrapolate them to make forecasts of the expected event*  
21 *magnitudes as injection continues. Here we describe a shale gas site where this approach was used in*  
22 *real time to make operational decisions during hydraulic fracturing operations.*  
23 *Microseismic observations revealed the intersection between hydraulic fracturing and a pre-existing*  
24 *fault or fracture network that became seismically active. While “red light” events, requiring a pause to*  
25 *the injection program, occurred on several occasions, the observed event magnitudes fell within*  
26 *expected levels based on the extrapolated statistical models, and the levels of seismicity remained*  
27 *within acceptable limits as defined by the regulator. To date, induced seismicity has typically been*  
28 *regulated using retroactive Traffic Light Schemes. This study shows that the use of high quality*  
29 *microseismic observations to populate statistical models that forecast expected event magnitudes can*  
30 *provide a more effective approach.*

31

32

## 33 1. Introduction

34 Human-induced seismicity is becoming an increasingly controversial topic. It is well known  
35 that activities such as mining and water impoundment can lead to felt seismicity, but  
36 increasingly activities such as geothermal energy (Grigoli *et al.*, 2018), underground storage  
37 of waste such as CO<sub>2</sub> or water (Keranen *et al.*, 2014), production from conventional  
38 hydrocarbon reservoirs (e.g. Segall, 1989) and hydraulic stimulation of shale gas reservoirs  
39 (Bao and Eaton, 2016), are attracting concern from the public, regulators and operators.

40 The stimulation of fractures by injecting water at high-pressure is a technique used to create  
41 conductive fracture networks in low-permeability reservoir rocks. Hydraulic fracture  
42 stimulation is widely used in the commercial production of hydrocarbons, and also to develop  
43 engineered geothermal systems. Use of this method has become more prominent in the past  
44 decade, associated primarily with the shale gas boom (Wang and Krupnick, 2013) in North  
45 America.

46 If hydraulic fractures intersect a pre-existing fault that is near to its critical stress state, the  
47 increase in pore pressure can reduce the effective normal stress, declamping the fault and  
48 creating induced seismicity. Such cases are relatively rare: Atkinson *et al.* (2016) estimate  
49 that only 0.3% of wells in British Columbia and Alberta, a region with some of the highest  
50 levels of hydraulic fracturing-induced seismicity (HF-IS), are associated with induced events  
51 larger than magnitude 3. Nonetheless, the issue of induced seismicity is a concern for the  
52 petroleum and geothermal industries, and will likely be of concern to other nascent industries,  
53 such as carbon capture and storage, as well (e.g., Verdon, 2014).

54 Debate continues with regards to the most effective methods to mitigate HF-IS, and what  
55 regulations should be applied. To date, regulators have typically imposed Traffic Light  
56 Schemes (TLSs) whereby the operator reduces, pauses or stops injection if the magnitude of  
57 the largest event exceeds a specified threshold. TLS thresholds have varied significantly in  
58 different jurisdictions (Bosman *et al.*, 2006; Baisch *et al.*, 2019): for example, in Alberta the  
59 red light is set at  $M = 4$ , whereas in the United Kingdom (U.K.) the red light is set at  $M = 0.5$ ,  
60 a difference in earthquake moment of over 175,000 times.

61 The simple TLSs currently used by hydraulic fracturing regulators are essentially retroactive  
62 in nature, because the operator takes actions after an event has occurred. In some case studies,  
63 seismicity has been observed to continue, and increase in magnitude, after injection has  
64 ceased (e.g., Häring *et al.*, 2008; Clarke *et al.*, 2014). These post-injection increased-  
65 magnitude events, known as “trailing events”, pose an issue for TLSs because they compel



66 the regulator to set thresholds that may be substantially lower than the actual magnitude they  
67 wish to avoid. Hence operations may be stopped even though levels of seismicity are well  
68 below that which might be considered hazardous.

69 It is therefore desirable to manage and mitigate induced seismicity in real time, as operations  
70 proceed. For example, injection volumes or pressures could be reduced (e.g., Kwiatek et al.,  
71 2019), or stimulation can be directed away from areas showing fault reactivation. Here we  
72 show a successful example of managing HF-IS with a recently acquired dataset from a shale  
73 gas operation in the UK.

74

### 75 **1.1 Using microseismic data for decision-making to mitigate induced seismicity**

76 The TLSs described by Bosman et al. (2016) and Baisch et al. (2019) that are currently used  
77 to regulate hydraulic fracturing stipulate decisions based solely on the magnitude of the  
78 largest events. This is a rational option if monitoring is provided by national or regional  
79 seismometer networks, where monitoring stations may be 10s of km from the site (e.g.,  
80 Clarke *et al.*, 2014; Friberg *et al.*, 2014; Skoumal *et al.*, 2015; Schultz *et al.*, 2015). In such  
81 cases only the larger events may be detected, and hypocentral locations and focal mechanisms  
82 may be poorly constrained. Hence the only reliable, well-constrained data are the magnitudes  
83 of the larger events.

84 However, it is not uncommon for operators to deploy microseismic monitoring, where  
85 downhole geophone arrays (Maxwell *et al.*, 2010) or dense surface arrays (Chambers *et al.*,  
86 2010) are able to detect very low magnitude “microseismic” events. High-quality  
87 microseismic monitoring may record thousands or even hundreds of thousands of events with  
88 very precise locations, spanning several orders of magnitude, provided in real time during  
89 operations (e.g., Zinno et al., 1998). These data will be highly relevant for understanding the  
90 risks posed by HF-IS. However, such data is not utilized by the relatively simple TLSs  
91 currently being applied by hydraulic fracturing regulators (Bosman et al., 2016).

92 There are two primary ways by which microseismic observations can be used to guide  
93 decisions to mitigate induced seismicity. Firstly, microseismic data can be used to detect and  
94 characterise the interactions between hydraulic fractures and pre-existing faults (Maxwell *et*  
95 *al.*, 2008; Maxwell *et al.*, 2009; Wessels *et al.*, 2011; Kettlety *et al.*, 2019; Igonin *et al.*, 2019;  
96 Eyre et al., 2019). Microseismic events during hydraulic fracturing typically occur in clusters  
97 extending from the well perpendicular to the minimum horizontal stress, tracking the growth  
98 of the hydraulic fractures and mapping the extent of the stimulated reservoir volume. If a fault

99 is intersected events may begin to line up along the structure, allowing it to be identified and  
100 mapped (e.g., Maxwell *et al.*, 2008; Wessels *et al.*, 2011; Hammack *et al.*, 2014; Kettlety *et*  
101 *al.*, 2019 Igonin *et al.*, 2019; Eyre *et al.*, 2019). In many cases fault reactivation can also be  
102 identified by a decrease in Gutenberg and Richter (1944) *b* values (e.g., Maxwell *et al.*, 2009;  
103 Verdon and Budge, 2018; Kettlety *et al.*, 2019), or by an increase in the rate of  
104 microseismicity relative to the injection rate (e.g., Maxwell *et al.*, 2008; Verdon and Budge,  
105 2018).

106 If a fault is identified during injection, then an operator can re-design their injection program  
107 to avoid further interacting with the fault. This can be achieved, for example: by skipping  
108 stages along a horizontal well; by changing the planned injection rates or volumes; or by  
109 altering the properties of the injected fluid (for example a more viscous fluid will carry more  
110 proppant while travelling less distance into the formation). Alternatively, Hofmann *et al.*  
111 (2018) have proposed adopting a “cyclic soft stimulation” program, where repeated injection  
112 is conducted at significantly lower rates. Zang *et al.* (2019) have demonstrated this approach  
113 for experimental-scale injection tests. However, the results from application to an industrial-  
114 scale project (Hofmann *et al.*, 2019) are more ambiguous, as the Pohang geothermal project,  
115 South Korea, at which this method was applied, went on to experience one of the largest  
116 injection-induced events ever recorded (Grigoli *et al.*, 2018). Moreover, for shale gas  
117 hydraulic fracturing applications, it is not clear that such a low-rate injection program would  
118 result in effective proppant placement into a shale formation.

119 Microseismic data can also be used to make forecasts of the expected event magnitudes  
120 during stimulation. Induced seismicity has been observed to follow the Gutenberg and Richter  
121 (G-R hereafter) distribution (van der Elst *et al.*, 2016), with the total number of events  
122 (Shapiro *et al.*, 2010; Mignan *et al.*, 2017) or the cumulative seismic moment released (Hallo  
123 *et al.*, 2014) being scaled to the cumulative injection volume. As such, expected event  
124 magnitudes can be forecast by characterising these relationships for the site in question, and  
125 then extrapolating them to the planned injection volume. This approach has shown significant  
126 promise when applied in a pseudo-prospective manner (e.g., Verdon and Budge, 2018).

127 These concepts have produced more advanced approaches to mitigate induced seismicity. For  
128 example, Mignan *et al.*, (2017) propose an adaptive Traffic Light Scheme (ATLS), whereby  
129 the daily rate of seismicity is scaled to the injection rate (as per Shapiro *et al.* (2010)), with  
130 the addition of a post-injection relaxation time that describes trailing effects. Event  
131 magnitudes are then determined from a G-R distribution, from which risk-based decisions can  
132 be made. Broccardo *et al.* (2017) extended the Mignan *et al.* (2017) approach by providing a

133 Bayesian framework within which the key parameters can be estimated. However, to our  
134 knowledge this approach has not yet been applied in real time to an active project.

135 Kwiatek *et al.* (2019) present an example of such methods being applied in real time to a deep  
136 geothermal project near Helsinki, Finland. They found that the observed seismicity scaled  
137 with injection parameters, allowing them to adjust the injection program to ensure that the  
138 levels of seismicity remained within the limits imposed by the regulator. The success of the  
139 type of approach demonstrated by Kwiatek *et al.* (2019), and the continued refinement of  
140 proposed adaptive TLSs (e.g., Mignan *et al.*, 2017; Broccardo *et al.*, 2017), provides the  
141 opportunity to move beyond the simple TLSs currently in common usage. However, their  
142 effectiveness must be demonstrated extensively in real time scenarios such that regulators  
143 gain confidence in their application.

144

## 145 **1.2 A case study from northwest England**

146 In this paper we report on the Preston New Road PNR-1z well, Lancashire, U.K., operated by  
147 Cuadrilla Resources Ltd (CRL hereafter). This was the first U.K. onshore well to be  
148 hydraulically fractured since a government review of HF-IS seismicity was concluded in  
149 2012. As such it is the subject of regular national media attention (e.g., Webster, 2018) and  
150 debate in the national parliament (Hansard, 2018). Given the high levels of public scrutiny,  
151 the site was extensively monitored both by CRL, and by independently-funded organisations  
152 such as the British Geological Survey (BGS). This monitoring included groundwater, surface  
153 water, air quality, and traffic movements, as well as the induced seismicity monitoring  
154 described here. Extensive baseline surveys were conducted for all of the above, so that any  
155 change from the pre-operational conditions could be identified.

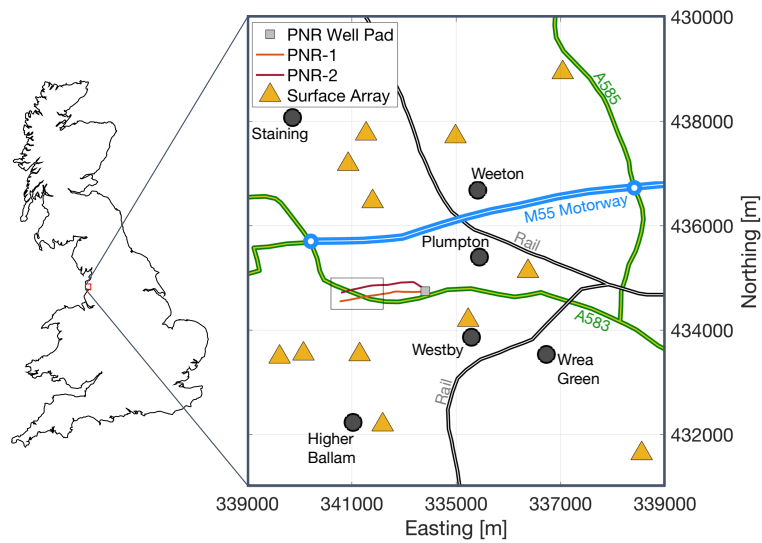
156 Given public concerns about HF-IS in the U.K., CRL took proactive measures to mitigate  
157 induced seismicity, guided by microseismic observations as outlined above. Here we provide  
158 a brief description of the operations conducted at the site, then show how microseismic data  
159 were used to identify and map the interaction between hydraulic fractures and a fault, and to  
160 forecast expected event magnitudes as the injection progressed. This information allowed  
161 CRL to adjust their injection program, ensuring that levels of seismicity did not exceed the  
162 overall objectives set by the regulator, as well as providing an increased understanding of  
163 more proactive measures that could be applied in future as alternatives to simplistic TLSs.

164

## 165 **2. Description of the Preston New Road Site**

166 The Preston New Road PNR-1z well targets the Carboniferous Lower Bowland Shale at a  
167 depth of approximately 2,300 m. The lateral portion of the well extends 780 m in a westward  
168 direction (Figure 1). A sliding-sleeve completion was used, with 41 individual sections  
169 spaced at 17.5 m intervals. CRL planned to stimulate each of these sleeves with 400 m<sup>3</sup> of  
170 slickwater, placing 50 tonnes of proppant per sleeve. Stimulation was carried out in two  
171 periods (Figure 2), firstly from 15<sup>th</sup> October to 2<sup>nd</sup> November, and then from 8<sup>th</sup> to 17<sup>th</sup>  
172 December 2018.

173

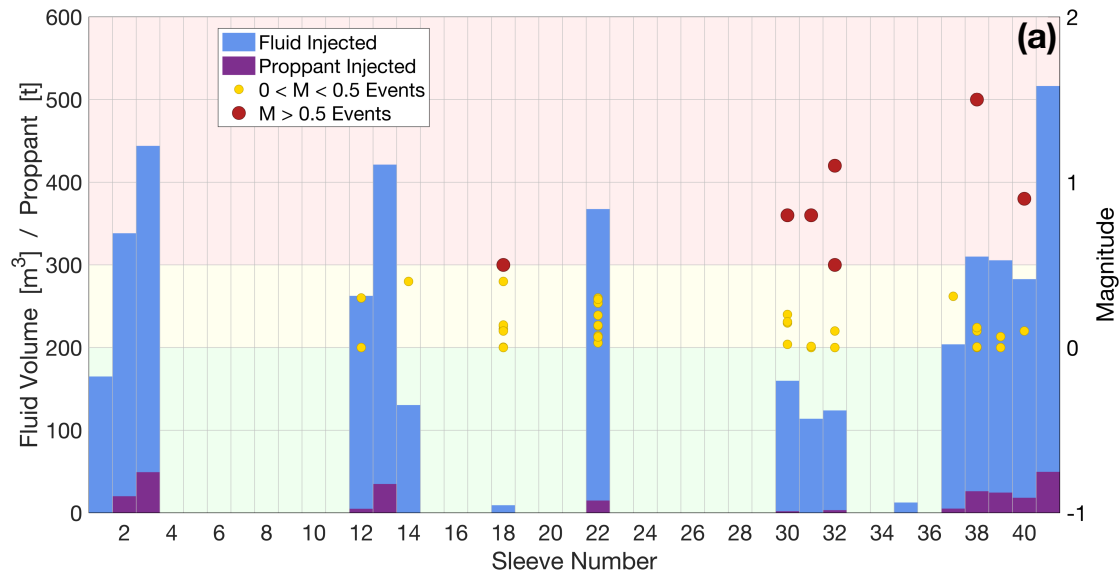


174

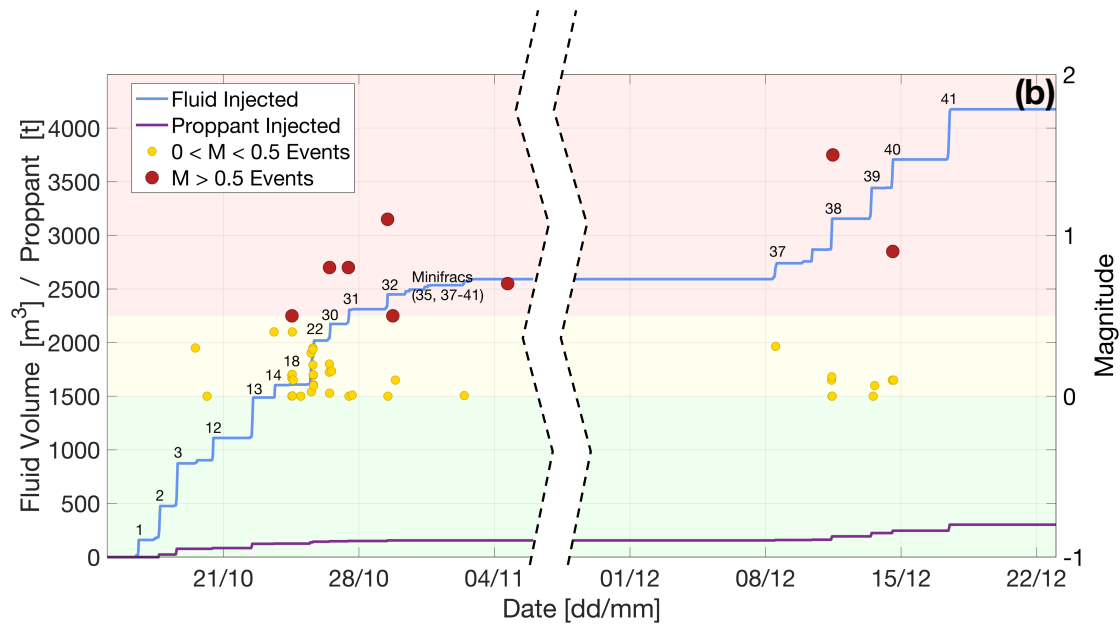
175 *Figure 1: Map of operations at Preston New Road showing the positions of the drilling pad*  
176 *and horizontal tracks of PNR-1z and PNR-2, and the positions of the surface monitoring*  
177 *stations. The black box marks the area of interest shown in subsequent figures. Major roads,*  
178 *rail links, and nearby villages are also marked. Coordinates are U.K. Grid Reference.*

179

180



181



182

183 *Figure 2: Overview of injection into PNR-1z. (a) shows the volume of fluid (blue) and mass of*  
 184 *proppant (purple) injected into each sleeve. It also shows all  $M > 0$  TLS events (yellow and*  
 185 *red dots) that occurred during or after injection into each sleeve. (b) shows cumulative fluid*  
 186 *volume (blue) and proppant mass (purple) injected as a function of time, again showing the*  
 187 *occurrence of TLS events. The numbering in (b) shows the sleeve being injected. The*  
 188 *background colours show the TLS green, amber and red magnitude thresholds.*

189

## 190 2.1 U.K. Regulations for Induced Seismicity

191 In the U.K., HF-IS is regulated by the Oil and Gas Authority (OGA). The OGA's objective is  
 192 to minimize the number of events felt at the surface by the public, and to avoid the possibility  
 193 of events capable of causing damage to nearby buildings or infrastructure (Oil and Gas

194 Authority, 2018). U.K. standards for ground vibrations from other activities such as quarry  
195 blasting, construction equipment and industrial machinery are provided by British Standard  
196 BS 7385-2. This sets a peak ground velocity (PGV) threshold, above which may cause  
197 cosmetic damage such as cracking of plaster, of 15 mm/s (at lower frequencies such as would  
198 be expected from induced seismicity). Using ground motion prediction equations (Akkar *et*  
199 *al.*, 2014), for hypocentral depths equivalent to expected depths of hydraulic fracturing and  
200 making conservative assumptions for ground conditions, this threshold is approximately  
201 equivalent to a magnitude of  $M = 3.5$ . Therefore, the OGA's objective could be reasonably  
202 translated as minimizing the number of events that have magnitudes  $2 < M < 3$ , and avoiding  
203 events that have magnitudes  $M > 3.5$ .

204 To regulate HF-IS the OGA currently applies a TLS with a red-light threshold of  $M = 0.5$   
205 (Green *et al.*, 2012), for which the operator must stop injection, reduce the pressure in the  
206 well, perform well integrity checks, and wait at least 18 hours before resuming injection. This  
207 is by some margin the most stringent level for ground motion applied to any industrial  
208 activity that we are aware of. The  $M = 0.5$  red-light threshold is 175 times smaller than the  $M$   
209  $= 2$  events that the scheme seeks to minimize, and over 30,000 times smaller than the  $M > 3.5$   
210 events that the scheme seeks to avoid. This disparity exists to mitigate the risk posed by  
211 trailing events, where event magnitudes may continue to increase after injection has been  
212 stopped (see Mignan *et al.* (2017) for an attempt to forecast trailing event populations). This  
213 TLS was applied to stimulation of the PNR-1z well, and the restrictive nature of this scheme  
214 had a significant impact on the operations: only 17 of the planned 41 stages were injected,  
215 and of these only 2 injected the 50 tonnes of proppant that was planned. However, only 2  
216 events were reported by the British Geological Survey (BGS) as being felt, and ground  
217 motions remained well below the levels at which damage might be expected. Therefore,  
218 overall the operation complied with the regulator's objective to minimise felt seismicity and  
219 avoid damaging seismicity.

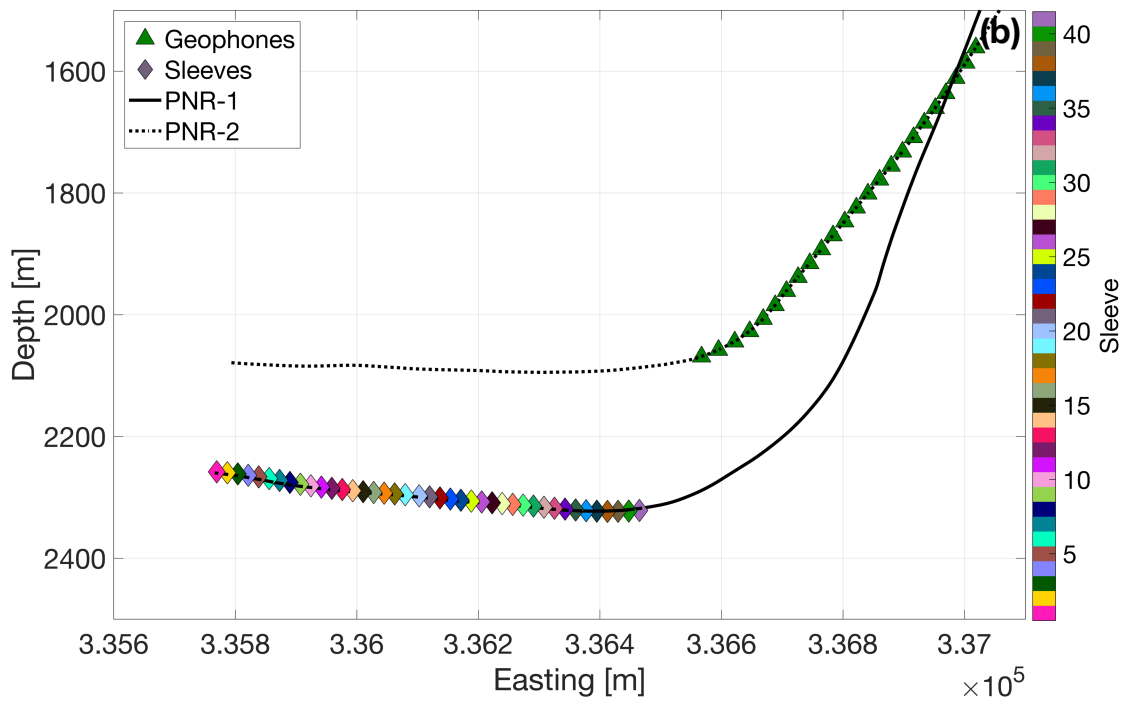
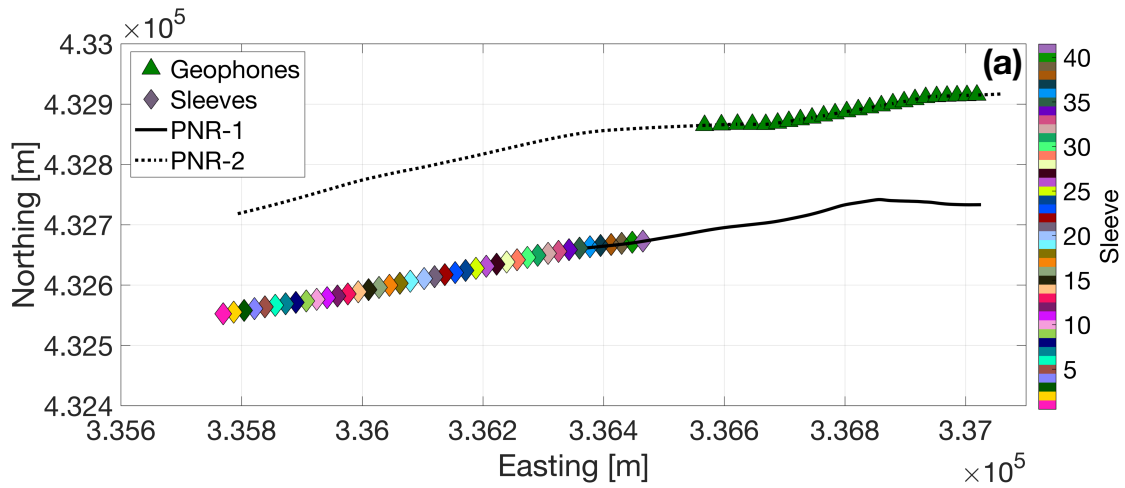
220

## 221 **2.2 Real time seismic and microseismic monitoring**

222 Two systems were used in combination to monitor induced seismicity at Preston New Road.  
223 Both of these systems provided event locations and magnitudes in real time (typically within  
224 1-4 minutes of event occurrence) computed by a processing contractor (Schlumberger). To  
225 administer the TLS an array of 8 sensors including 2 broadband seismometers and 6  
226 geophones (4.5 Hz instruments) was deployed at the surface, augmented by 4 broadband  
227 seismometers deployed by the BGS (Figure 1). During real time monitoring the surface array  
228 identified 54 events with a minimum magnitude of  $M_L = -0.8$ . The surface array provided

229 sufficient coverage such that focal mechanisms could be determined for 9 of the largest  
230 events during real time monitoring.

231 Microseismicity was recorded using an array of 24 geophones (15 Hz instruments) placed in  
232 the build section (where the well deviates from vertical to horizontal) of the adjacent PNR-2  
233 well, 200 m shallower and 220 m northeast of the nearest sleeve in PNR-1z (Figure 3). This  
234 array reported over 39,000 events in real time, with a minimum magnitude of  $M_w = -3.0$ .



237 *Figure 3: Map (a) and cross-section (b) of the downhole monitoring array deployed in well*  
238 *PNR-2, and the sleeves through which injection was conducted in PNR-1z.*

239

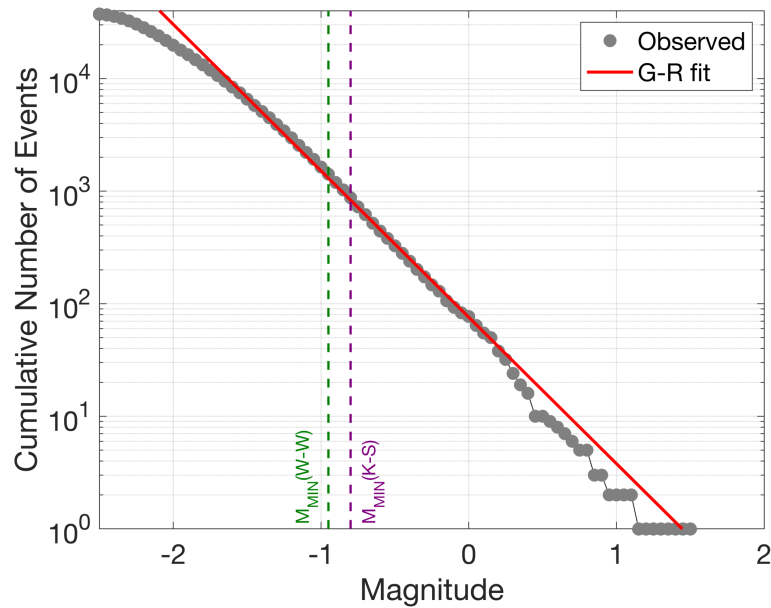
## 240 2.3 A note on magnitudes

241 Measurements of magnitudes for small events can be challenging (Kendall *et al.*, 2019). Two  
242 different magnitude scales were in use during real time operations at Preston New Road. The  
243 U.K. TLS regulations mandate the use of a local magnitude scale with a correction applied to  
244 account for the small source-receiver distances (Butcher *et al.*, 2017; Luckett *et al.*, 2019).  
245 Therefore, magnitudes from the surface array were reported as  $M_L$  values. However, these  $M_L$   
246 scales are calibrated using surface stations, implicitly including free-surface effects and near-  
247 surface attenuation, so this  $M_L$  scale is not calibrated for downhole instruments. Instead the  
248 downhole events were reported as  $M_W$  values. While a direct comparison and conversion  
249 between the two scales might seem like an obvious solution (e.g. Edwards and Douglas,  
250 2014), in practice this was more challenging. The surface array recorded the largest 54 events,  
251 so only these events had reported  $M_L$  values. However, many of these larger events produced  
252 subsurface motions that were beyond the dynamic range of the downhole instruments, and so  
253 accurate downhole  $M_W$  values could not be determined for these events. Hence, there is only a  
254 small subset of events which are large enough such that a robust  $M_W$  value can be computed  
255 using the surface array, but not too large such that a robust  $M_W$  value can also be computed  
256 using the downhole stations, thereby enabling a comparison to be made.

257 Work is ongoing to resolve the observed  $M_L$  and  $M_W$  values. However, the need for rapid  
258 decision-making meant that this information was not used during real time operations.  
259 Instead, we used  $M_L$  values for the 54 events that were reported by the surface array, and  $M_W$   
260 values for the remaining events. Clearly this solution was far from optimal. However, we note  
261 that doing so does not produce anomalies or unusual behaviour if the overall magnitude-  
262 frequency distribution is examined (Figure 4), suggesting that this approach was reasonable in  
263 this case. However, in future cases this issue should be addressed by ensuring that moment  
264 magnitudes are reported by both array types, and that relationships to convert between  
265 downhole  $M_W$  values and surface  $M_L$  values are calibrated. In Figure 4 we fit a G-R  
266 distribution to entire event catalogue using the Aki (1965) maximum likelihood approach,  
267 computing the magnitude of completeness,  $M_{MIN}$ , using both the Wiemer and Wyss (2000)  
268 formulation with an acceptance threshold of 95%, which gave  $M_{MIN} = -0.95$ , and by using a  
269 Kolmogorov-Smirnov test with a 10% significance threshold (e.g., Clauset *et al.*, 2009;  
270 Williams and Le Calvez, 2013), which gave  $M_{MIN} = -0.8$ . In both cases, the resulting G-R  
271 parameters were  $a = 1.9$  and  $b = 1.3$ .

272





273

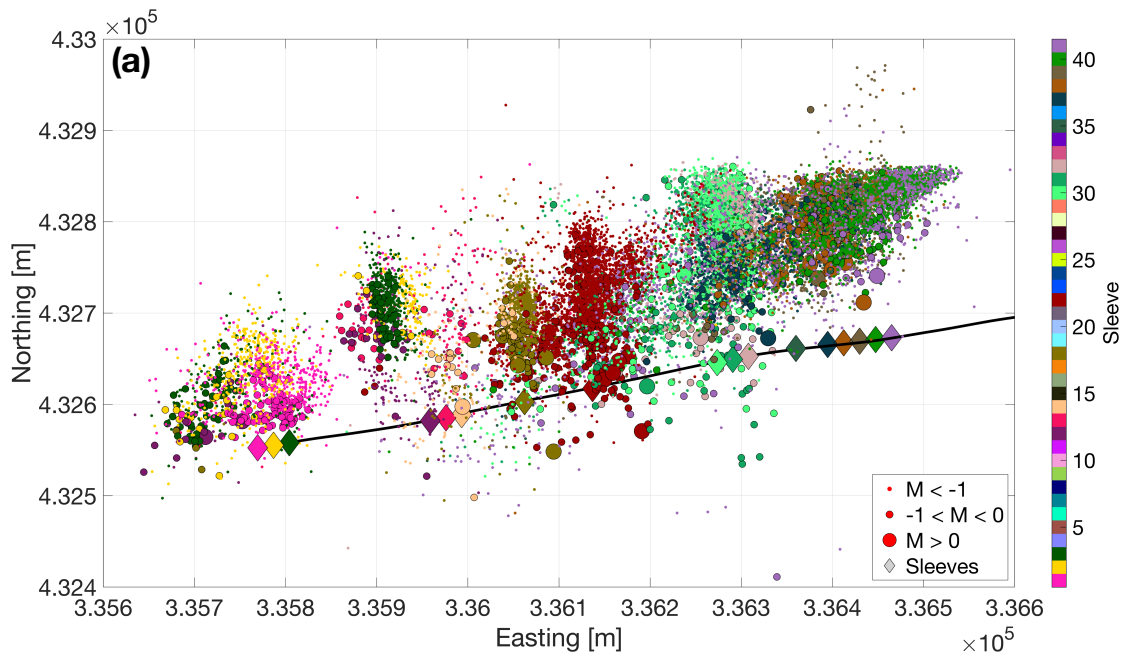
274 *Figure 4: Magnitude-frequency distribution for all events reported in real time (grey dots).*  
 275 *The observed distribution follows the G-R distribution with  $a = 1.9$  and  $b = 1.3$  (red line). We*  
 276 *use both the Wiemer and Wyss (2000) formulation (green dashed line) and a Kolmogorov-*  
 277 *Smirnov test (purple dashed line) to assess the overall magnitude of completeness.*

278

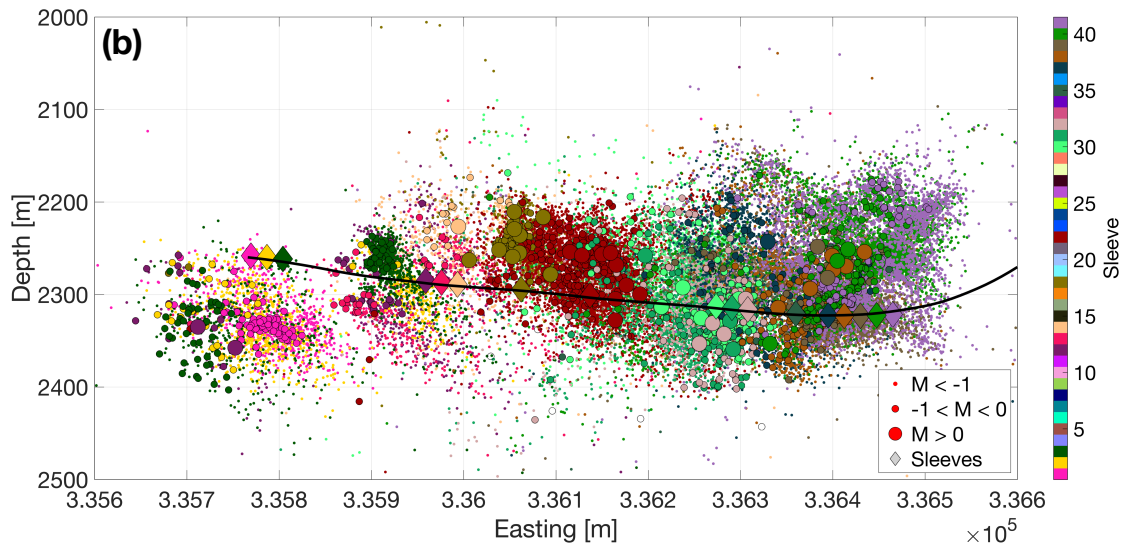
### 279 **3. Microseismic observations**

280 Figure 5 shows a map and cross-section for located events with a signal-to-noise ratio greater  
 281 than 5. Events during each stage are mostly found in the vicinity of the corresponding  
 282 injection sleeve, extending approximately 200 m to the north. The events extend  
 283 approximately 150 m above and below the well, remaining within the Bowland Shale  
 284 Formation. The largest observed event has a magnitude of  $M = 1.5$ , and in total 8 events  
 285 exceeded the TLS  $M = 0.5$  threshold, 3 of these occurred during injection and required  
 286 pumping to be stopped, while the remaining 5 were trailing events that occurred after  
 287 injection had ceased.

288



289



290

291 *Figure 5: Map view (a) and cross-section (b) of microseismic events detected during real time*  
 292 *monitoring at PNR-1z. Events are coloured by the sleeve number with which they are*  
 293 *associated. The PNR-1z well profile is shown by the black line.*

294

### 295 3.1. Relationship between microseismicity and previously-observed faults

296 Prior to the start of operations, a 3D reflection seismic survey was acquired at the site. Several  
 297 pre-existing faults and “seismic discontinuities” (potential small faults that are at the limit of  
 298 resolution for 3D seismic surveys) were identified (Cuadrilla Resources Ltd., 2018). We  
 299 observed little or no correlation between the positions of these features the and  
 300 microseismicity. The events associated with Stages 1 – 3 at the toe of the well overlap with  
 301 one of the seismic discontinuities. However, the levels of microseismicity produced by these

302 stages were among the lowest. In contrast, none of the events that exceeded the  $M > 0.5$  TLS  
303 threshold occurred on structures identified from the 3D survey.

304 Indeed, no microseismicity coincided with any of the large faults identified in the 3D seismic  
305 survey, all of which were significantly further from the well than the greatest distances  
306 reached by the microseismicity. This observation allowed CRL to proceed with confidence  
307 that the hydraulic stimulation was unlikely to cause re-activation of the larger faults that had  
308 been identified.

309

### 310 **3.2. Identification of potential seismogenic structures**

311 The northwards propagation of microseismicity from each injection sleeve traces the  
312 propagation of hydraulic fractures perpendicular to the minimum horizontal stress azimuth of  
313 approximately  $80^\circ$  (Fellgett *et al.*, 2017). However, our interest was to identify pre-existing  
314 structures on which the larger events may occur. We note that the largest event, with a  
315 magnitude of  $M = 1.5$ , could correspond to a rupture with displacement of less than 1 cm with  
316 a length less than 100 m. At this scale the distinction between a “small fault” and a “large  
317 fracture” is somewhat arbitrary: we will use “fault” hereafter to describe such features, while  
318 keeping this fact in mind.

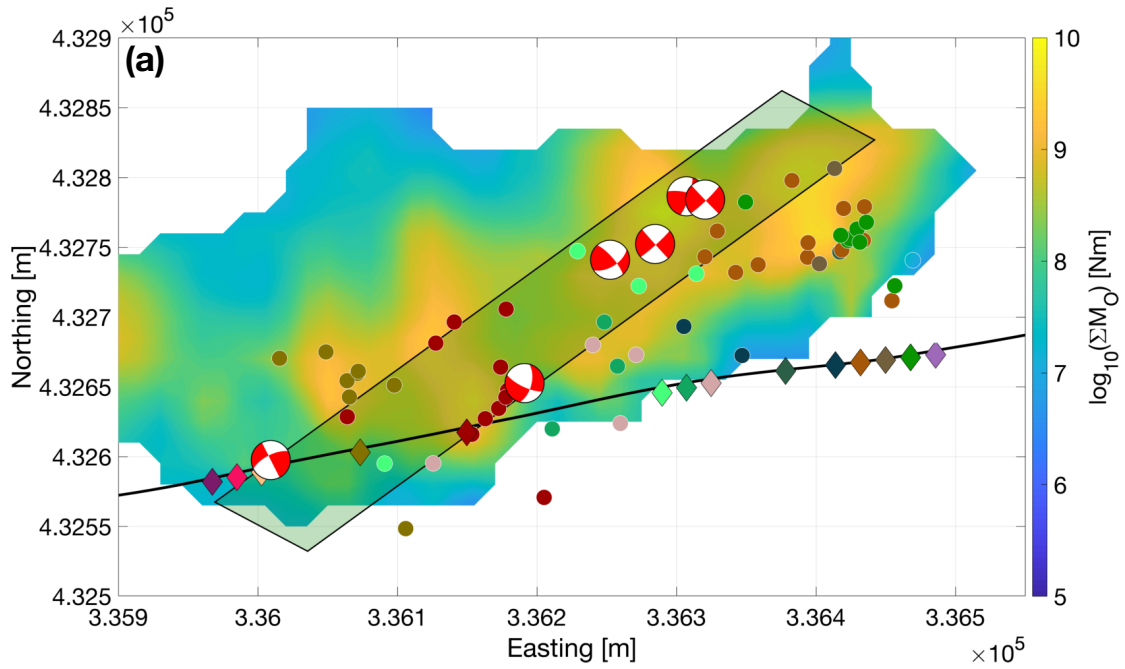
319 In Figure 5 the events do not display an obvious alignment along a pre-existing fault, an  
320 observation which often provides the clearest evidence of fault reactivation (e.g., Igonin *et al.*,  
321 2019; Kettlety *et al.*, 2019; Eyre *et al.*, 2019). Instead, we use a combination of observations  
322 to identify and define the seismogenic structures responsible for the largest events.

323

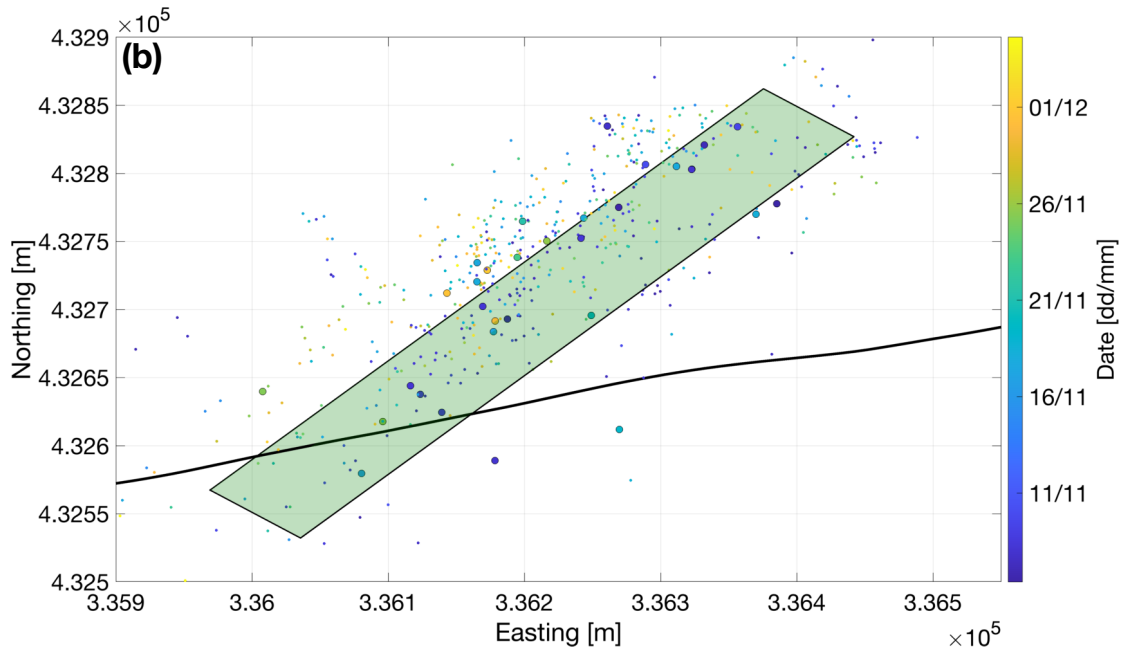
### 324 **3.3. Focal mechanisms**

325 The focal mechanisms for 6 of the largest events are shown in Figure 6a. The events all have  
326 similar mechanisms: either left-lateral strike slip on a near-vertical fault striking NE-SW, or  
327 right-lateral strike-slip on a near-vertical fault striking NW-SE. The consistent orientation of  
328 these focal mechanisms provides a constraint for the orientation of any potential seismogenic  
329 structure.

330



331



332

333 *Figure 6: Maps showing the observations used to identify seismogenic structures. (a) shows*  
 334 *all events with  $M > 0$  (dots coloured by sleeve number as per Figure 5), the cumulative*  
 335 *seismic moment (contours), and the focal mechanisms of the largest events. (b) shows a map*  
 336 *of the events that occurred during the injection hiatus from 3<sup>rd</sup> November to 7<sup>th</sup> December. We*  
 337 *combine the largest events and the injection hiatus events to map a plane striking at  $237^\circ$  and*  
 338 *dipping at  $70^\circ$  (black-outlined box).*

339

340 **3.4. Mapping large events and cumulative moment release**

341 Figure 6a also shows the positions of all events with  $M > 0$ , and maps the cumulative seismic  
342 moment release,  $\Sigma M_0$ . These observations allow us to identify a single zone in which almost  
343 all of the larger events were occurring, and within which the overall cumulative seismic  
344 moment release was highest. This zone intersects the PNR-1z well at roughly the position of  
345 Sleeve 18, which was the first stage on which an event exceeding the  $M > 0.5$  TLS threshold  
346 occurred. Interaction between injection activities and this zone occurred along the well  
347 towards the heel. Importantly, the orientation of this zone matches the orientation of the NE-  
348 SW plane of the observed focal mechanisms.

349

### 350 **3.5. Microseismicity during injection hiatus**

351 These observations allowed us to identify the seismogenic feature during the initial  
352 stimulation of Stages 18 – 41 in October 2018 (Figure 2). From the 3<sup>rd</sup> of November, CRL  
353 paused the injection program in response to repeated  $M > 0.5$  events that had occurred during  
354 the previous week. The injection pause continued until 7<sup>th</sup> December. Observations of  
355 microseismicity during this injection hiatus (Figure 6b) provided the final and definitive  
356 identification of the seismogenic structure. The events during hiatus, almost all of which had  
357 magnitudes less than  $M < -1$ , were all located along the same feature that we had identified  
358 from the focal mechanism orientations, the positions of the largest events, and the cumulative  
359 moment release map.

360 Our overall interpretation of the observed microseismicity is that a pre-existing fault plane  
361 runs northeast from the well. During hydraulic stimulation, larger events occurred when the  
362 hydraulic fractures from each stage intersected this fault. During the hiatus, whereas the  
363 microseismic events associated with hydraulic fracturing stopped, low levels of  
364 microseismicity continued to persist along this feature for a longer period of time. We fit a  
365 plane to a combined population of the  $M > 0$  events (Figure 6a) and the hiatus events (Figure  
366 6b), by finding the plane that minimises the least-squares distance between each event and the  
367 plane. We found a strike of  $237^\circ$  and a dip of  $70^\circ$ , which is consistent with the observed focal  
368 mechanisms. We term this fault NEF-1 (Northeast Fault-1) hereafter. With the maximum and  
369 minimum horizontal stresses oriented north-south and east-west respectively, this plane is  
370 well-oriented for the observed left-lateral strike slip motion, and the observed focal  
371 mechanisms are therefore consistent with the local stress conditions.

372

## 373 **4. Statistical Forecasting of Event Magnitudes**

374 During stimulation we applied in real time an event magnitude forecasting model to guide  
 375 operational decisions with respect to induced seismicity. Hallo *et al.* (2014) introduced the  
 376 concept of seismic efficiency,  $S_{EFF}$ , which describes the correlation between the cumulative  
 377 moment release,  $\Sigma M_O$ , and the cumulative injection volume  $\Delta V$ :

$$378 \quad S_{EFF} = \frac{\Sigma M_O}{\mu \Delta V}, \quad (1)$$

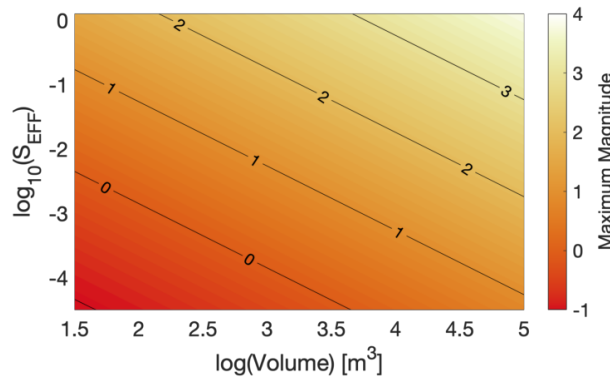
379 where  $\mu$  is the shear modulus, assumed to be 20 GPa here. Based on the observed values of  
 380  $S_{EFF}$  and the  $b$  value, the size of the largest expected event,  $M_{MAX}$  can be estimated as:

$$381 \quad M_{MAX} = \frac{2}{3} \left( \log_{10} \left( \frac{S_{EFF} \mu \Delta V^{\frac{3-b}{2}}}{b 10^{9.1}} \right) \right) + \frac{2}{3} \log_{10} (10^{b\delta} - 10^{-b\delta}), \quad (2)$$

382 where  $\delta$  is the probabilistic half-bin size defined around  $M_{MAX}$  (Hallo *et al.*, 2014). This  
 383 formulation assumes that  $b$  and  $S_{EFF}$  do not change significantly for a given stage, or for a  
 384 given volume of rock being stimulated. Verdon and Budge (2018) applied this approach in a  
 385 pseudo-prospective manner to a hydraulic fracturing dataset from the Horn River Shale,  
 386 Canada, showing that it would have accurately forecast event magnitudes had it been applied  
 387 in real time.

388 Equation 2 posits a logarithmic dependence between injection volume and the largest event  
 389 size. Given that the planned injection volumes do not vary by orders of magnitude between  
 390 stages, the primary controlling factor on the largest event magnitude is therefore  $S_{EFF}$ . The  
 391 relationship between  $S_{EFF}$ ,  $\Delta V$ , and  $M_{MAX}$  is plotted in Figure 7 (assuming  $b = 1$ ).

392



393

394 *Figure 7: Relationship between  $S_{EFF}$ ,  $\Delta V$ , and  $M_{MAX}$  given by Equation 2 (assuming  $b = 1$ ),*  
 395 *showing the logarithmic dependence of  $M_{MAX}$  on  $\Delta V$ .*

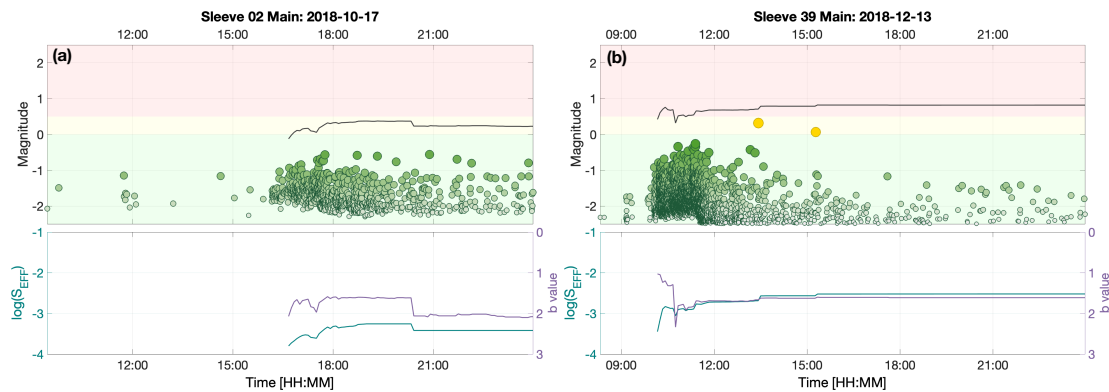
396

397 Equation (2) provides the most likely maximum event magnitude. In practice it is more useful  
 398 to define a value for  $M_{MAX}$  that is unlikely to be exceeded. Using synthetic event

399 distributions, Verdon and Budge (2018) showed that adding a value of 0.5 to Equation 2 is  
 400 sufficient to capture 95% of the variance between true and re-constructed model populations.  
 401 In our analysis we applied this correction such that our results provided a value that, within  
 402 reasonable levels of certainty, will not be exceeded.

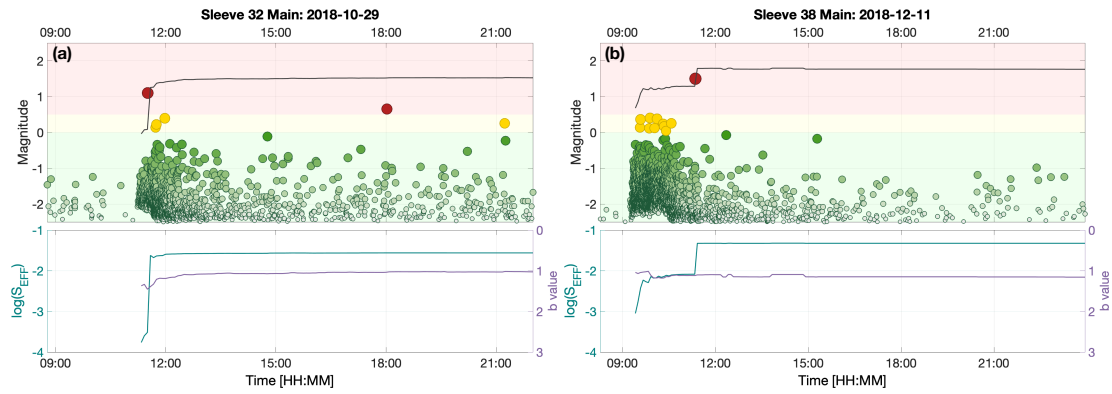
403 We tracked  $b$  and  $S_{EFF}$  in real time during every stage, providing regularly-updated forecasts  
 404 of  $M_{MAX}$ . We computed the  $b$  value using the Aki (1965) maximum likelihood approach,  
 405 finding the minimum completeness threshold using a Kolmogorov-Smirnov test at a 10%  
 406 acceptance level to assess the quality of fit between the observed magnitude distribution and  
 407 the G-R relationship (Clauset *et al.*, 2009; Williams and Le Calvez, 2013), requiring a  
 408 minimum of 50 events for a reliable measurement (though with over 39,000 events in 17  
 409 stages, the number of events passed this threshold very quickly for each stage).

410 Figure 8 shows a selection of results for this analysis when performed on a stage-by-stage  
 411 basis, i.e., considering  $\Sigma M_O$  and  $\Delta V$  associated with each individual stage. We find that for  
 412 most of the stages this approach provided accurate bounds, with the observed events falling  
 413 within the modelled value of  $M_{MAX}$ . However, this is not always the case, as can be seen for  
 414 Stages 32 and 38 in Figure 9, for example.



415

416 *Figure 8: Examples of  $S_{EFF}$ ,  $b$ , and  $M_{MAX}$  tracked during injection on a stage-by-stage basis.*  
 417 *In the lower panels we track  $S_{EFF}$  (blue) and  $b$  (purple), and in the upper panels we plot the*  
 418 *resulting values of  $M_{MAX}$  (black line) compared against observed events (circles coloured by*  
 419 *magnitude relative to the TLS thresholds).*



420

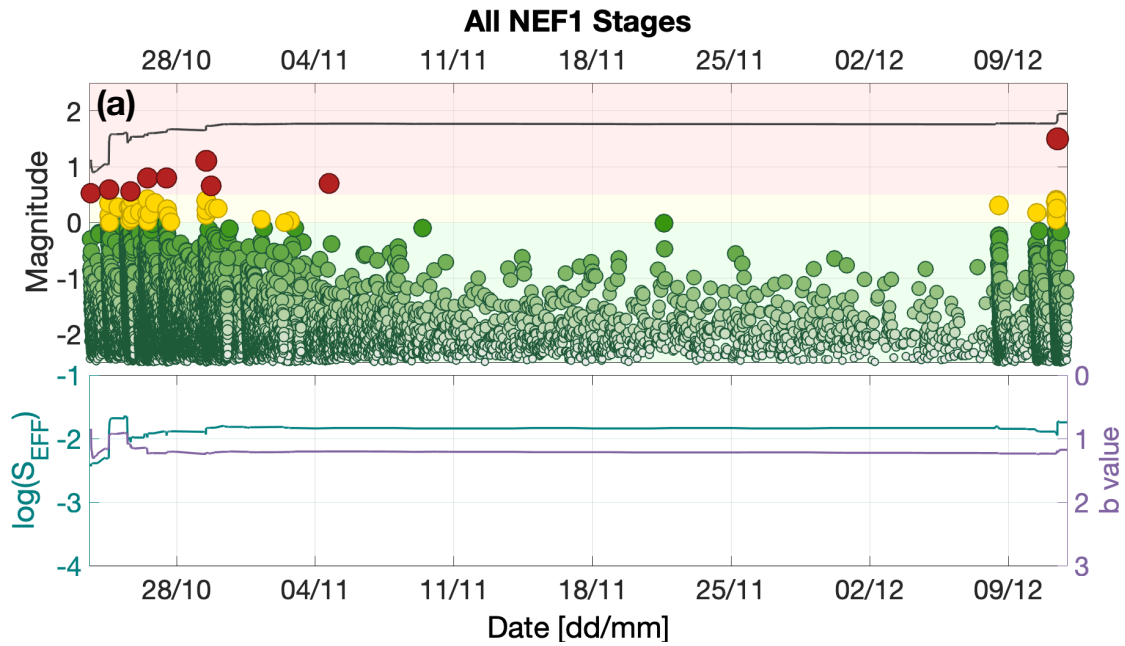
421 *Figure 9: Examples of  $S_{EFF}$ ,  $b$ , and  $M_{MAX}$  tracked during injection on a stage-by-stage basis,*  
 422 *in the same format as Figure 8. For some stages, events occur that exceed the modelled*  
 423  *$M_{MAX}$  values, when the injection volumes and observed events are treated discretely on a*  
 424 *stage-by-stage basis.*

425

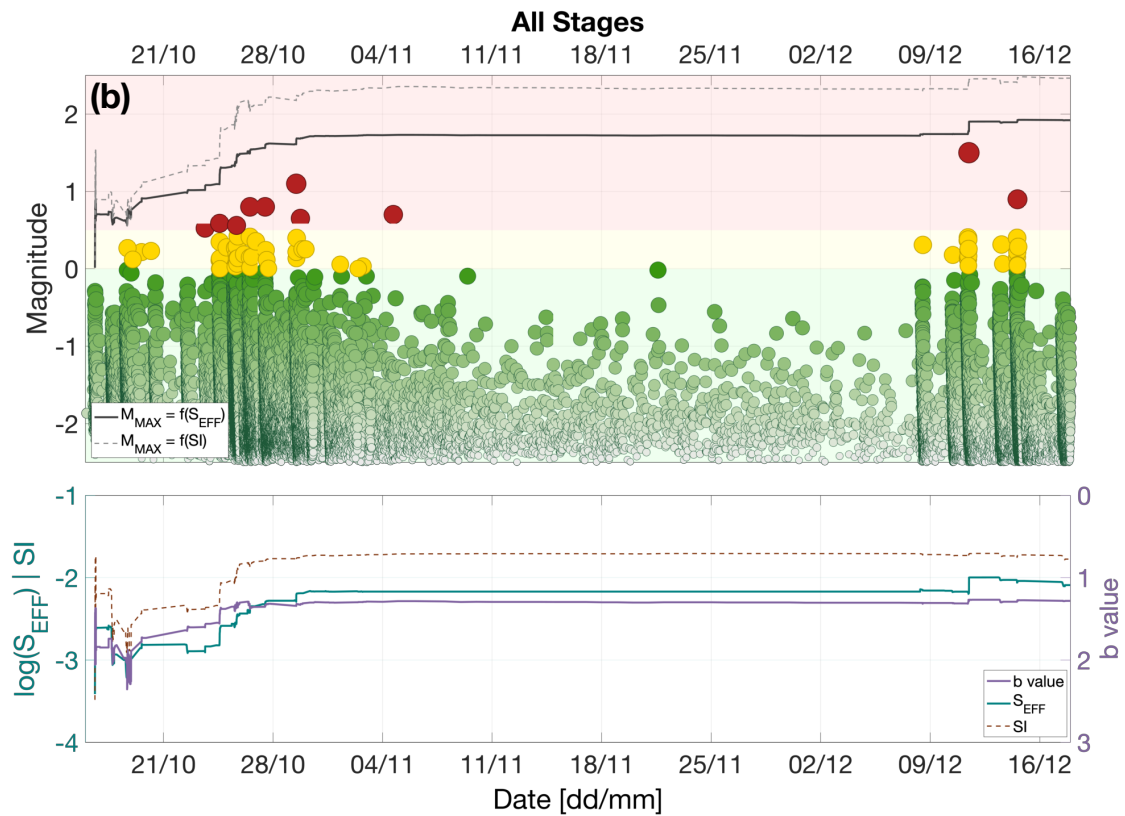
426 The reason for this discrepancy is obvious when considered in the light of the observations  
 427 and interpretations of the microseismicity presented in Section 3: the NEF-1 fault runs  
 428 obliquely to the well and was intersected by multiple stages. It is therefore not appropriate to  
 429 consider each stage independently because the seismicity was caused by repeated injection  
 430 into the same feature. Instead, as the NEF-1 feature was identified, we adjusted our approach  
 431 to include the effects of repeated injection, treating all injection and seismicity from Stage 18  
 432 onwards cumulatively (Figure 10a). The value of  $S_{EFF}$  was observed to stabilise very quickly  
 433 at a value of approximately  $\log_{10} S_{EFF} \approx -2$ , which produces a forecast  $M_{MAX}$  of 1.7. The  
 434 largest observed event at PNR-1z had a magnitude of  $M = 1.5$ .

435





436



437

438 *Figure 10: Forecasting  $M_{MAX}$  over cumulative stages. Here we treat stages cumulatively to*  
 439 *generate  $M_{MAX}$  forecasts when (a) all of the stages that intersect the NEF-1 fault are*  
 440 *considered, and (b) when all stages are considered. The observed  $S_{EFF}$  is initially at*  
 441 *approximately  $\log_{10} S_{EFF} \approx -3$ , giving a forecast  $M_{MAX} < 1$ . As the injection begins to*  
 442 *interact with the NEF-1 feature, the b value decreases and the overall seismic efficiency*  
 443 *increases to approximately  $\log_{10} S_{EFF} \approx -2$ , giving a forecast  $M_{MAX} < 2$ . In (b) we also*

444 *show the Shapiro et al. (2010) seismogenic index (gold dashed line), and the resulting  $M_{MAX}$*   
445 *forecast from this approach (grey dashed line).*

446

447 For completeness, we also considered the cumulative impacts of the full injection volume and  
448 seismicity from all the injection stages (Figure 10b). This represents the worst-case scenario if  
449 all of the injected fluid was inducing events on a single seismogenic feature. Initial values for  
450  $S_{EFF}$  are low ( $\log_{10} S_{EFF} \approx -3$ ) and  $b$  values are high ( $b > 1.5$ ) giving  $M_{MAX} < 1$ . From  
451 Stage 18 onwards we observed the hydraulic fracturing interact with the NEF-1 fault,  
452 producing an increase in  $S_{EFF}$  to ( $\log_{10} S_{EFF} \approx -2$ ) and a decrease in  $b$  to approximately 1.  
453 This produces an increase in  $M_{MAX}$  to  $M_{MAX} \approx 2$ .

454

## 455 **5. Discussion**

### 456 **5.1. Operational Decision-Making**

457 The observations presented above were used by CRL to guide their operational decision-  
458 making, especially during the latter injection stages in December, after the period of injection  
459 hiatus in November 2018.

460 During hydraulic fracturing, placement of the proppant cannot begin until fracture breakdown  
461 has occurred and fractures begin to propagate. This typically requires a minimum of  
462 approximately 80 m<sup>3</sup> of fluid. The proppant concentration is then gradually increased as the  
463 injection continues, such that the majority of proppant is placed at the end of the stage. If a  
464 stage is terminated mid-way through by a TLS red-light event, only a small proportion of the  
465 proppant will have been placed, even if several hundred m<sup>3</sup> of fluid has been injected. In  
466 effect, the stage will therefore have been wasted and the environmental water use and seismic  
467 risk unnecessarily increased.

468 At PNR-1z, the modelling described above showed that events larger than  $M = 2$  were not  
469 expected on the NEF-1 fault given the observed  $b$  values and seismic efficiency, and the  
470 planned injection program. This forecast was reported to the OGA in November 2018, and it  
471 falls within the objectives of seismicity mitigation set out by the OGA (minimising felt events  
472 and avoiding damaging events). However, the NEF-1 fault could be expected to continue  
473 producing  $M > 0.5$  red-light events that would terminate injection, preventing the placement  
474 of proppant. CRL therefore decided that further injection into the sleeves that intersect the  
475 NEF-1 fault would be wasted, and in December 2018 they restarted injection in Stages 37 –  
476 41 at the heel of the well. Based on the seismicity mapping described in Section 3 it was  
477 hoped that these stages would pass to the east of the NEF-1 fault, allowing stages to be

478 completed without interruption. Based on the forecasting described in Section 4, CRL was  
479 able to do so with confidence if these stages did intersect NEF-1, the levels of seismicity  
480 would not exceed the objectives set by the OGA, and therefore injection could be conducted  
481 safely.

482 In reality, some of these latter stages did intersect the NEF-1 fault, triggering two further TLS  
483 events with  $M > 0.5$ . However, the event magnitudes remained within the levels that had been  
484 forecast, as described in the section above, and within the overall regulatory objective to  
485 minimise the number of felt events.

486

## 487 **5.2. Seismic Efficiency and Seismogenic Index**

488 The Seismogenic Index,  $SI$  (Shapiro *et al.*, 2010), is another parameter that is commonly used  
489 to describe the relationship between injected volume and seismicity. Whereas the  $S_{EFF}$   
490 parameter we use here scales the injection volume to the cumulative seismic moment release,  
491 the seismogenic index scales the injection volume to the number of events larger than a given  
492 magnitude. Since many previous studies have provided estimates of  $SI$ , it is of interest to  
493 compute this parameter for the PNR-1z dataset to facilitate a comparison. Our results are  
494 shown alongside the  $S_{EFF}$  results in Figure 10, and we also plot the  $M_{MAX}$  forecasts that result  
495 (at 5% probability of exceedance level) using the method described by Shapiro *et al.* (2010).  
496 We note that, as found by Verdon and Budge (2018),  $SI$  follows a similar trend to  $\log_{10} S_{EFF}$ ,  
497 which is not surprising because the total moment release will depend on the number of events  
498 that occur. We also find that the  $M_{MAX}$  values derived from the  $SI$  measurements are larger  
499 than those derived from the  $S_{EFF}$  measurements, as also found by Verdon and Budge (2018).

500 Dinske and Shapiro (2013) catalogue  $SI$  values for a range of injection sites, finding values  
501 ranging from  $-9 < SI < 1$ . The maximum value of  $SI$  obtained here is  $SI = -1.8$ , which is  
502 similar to many of the geothermal projects described by Dinske and Shapiro (2013), but  
503 significantly larger than those obtained for hydraulic fracturing sites at Cotton Valley (East  
504 Texas) and in the Barnett Shale (Northeast Texas). However, the values obtained for PNR-1z  
505 are similar to values found by Verdon and Budge (2018) for hydraulic fracturing in the Horn  
506 River Basin, British Columbia, Canada, where  $-4 < SI < -1$ , and towards the lower end of the  
507 range found by Schultz *et al.* (2018) for hydraulic fracturing sites in Alberta, Canada, where  
508  $-2.5 < SI < -0.5$ . The most notable past case of injection-induced seismicity in the U.K. for  
509 which  $SI$  values are available is the Rosemanowes Hot Dry Rock geothermal site, for which  
510 Li *et al.* (2018) found maximum values of  $SI = -3.4$ , significantly lower than the values found  
511 for PNR-1z.

512

### 513 5.3. Scaling between volume and cumulative moment release

514 The underlying assumption implicit to Equation (1) is that the cumulative seismic moment  
515 scales linearly with the injection volume. However, recent studies (e.g., Galis *et al.*, 2017; De  
516 Barros *et al.*, 2019) have proposed alternative scaling factors, and in particular that

$$517 \quad \Sigma M_O \propto V^{\frac{3}{2}}. \quad (3)$$

518 This scaling by an exponent of 1.5 is also implicit to the Shapiro *et al.* (2010) *SI* approach,  
519 since the logarithm of the seismic moment scales with  $1.5 \times M_W$ . Discussion continues as to  
520 the most appropriate value of the scaling exponent between  $\Sigma M_O$  and  $V$  (e.g., Chen *et al.*,  
521 2018; De Barros *et al.*, 2019).

522 In Figure 11a we track the evolution of the cumulative moment release with the cumulative  
523 injection volume, and estimate a least-squares fit (in log-log space) to these data for a  
524 relationship having the form

$$525 \quad \Sigma M_O = \alpha V^n. \quad (4)$$

526 Our results are shown in Figure 11a. For the overall dataset, we find a best-fit value of  $n =$   
527 1.6. However, it is apparent that the data may not be best described by a single value. Based  
528 on our observations of which stages caused reactivation of the NEF-1 fault, combined with  
529 apparent changes in slope of Figure 11a, we divide the data into 3 periods: Stages 1 – 14,  
530 prior to reactivation of the NEF-1 fault; Stages 18 – 38, while reactivation of the fault was  
531 taking place, and Stages 39 – 41 which appeared to miss the NEF-1 fault at the heel of the  
532 well. Doing so, we find best-fit values of  $n = 0.8$  for Stages 1 – 14;  $n = 3.0$  for Stages 18 – 38,  
533 and  $n = 0.6$  for Stages 39 – 41.

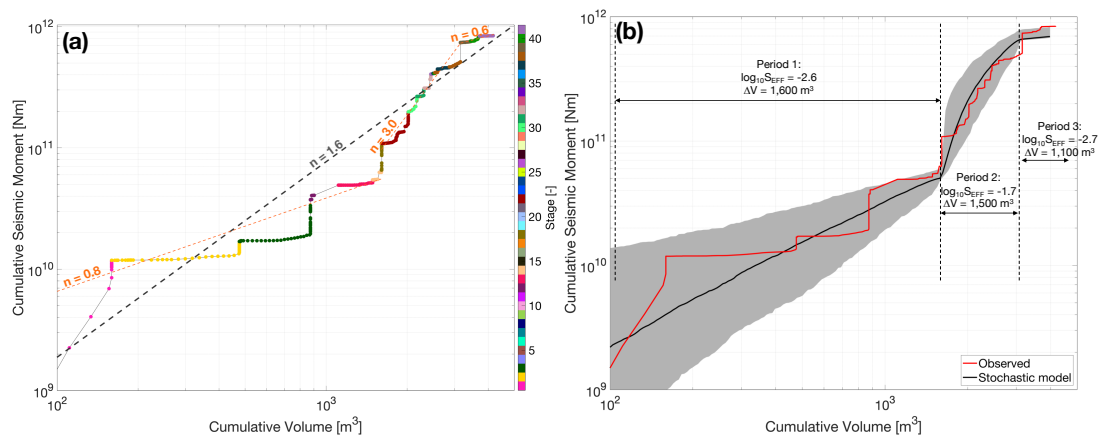
534 This variability highlights a challenge that arises when attempting to assess any scaling  
535 relationship between cumulative moment and volume, should the constant of proportionality  
536 ( $\alpha$  in Equation (4)) vary during the process, which might be expected as hydraulic fracturing  
537 proceeds along a horizontal well, and so encounters different volumes of rock that have  
538 different geomechanical properties.

539 We further demonstrate this effect in Figure 11b. Based on our observations in Section 4, we  
540 simulate a scenario whereby event populations are generated with  $b = 1.2$  and  $\log_{10} S_{EFF} = -$   
541 2.6 (assuming a linear relationship between  $V$  and  $\Sigma M_O$ ) for the first 1,600 m<sup>3</sup> of injection  
542 (representing Stages 1 – 14);  $\log_{10} S_{EFF} = -1.7$  for the second 1,500 m<sup>3</sup> of injection  
543 (representing Stages 18 – 38); and  $\log_{10} S_{EFF} = -2.7$  for the final 1,100 m<sup>3</sup> of injection  
544 (representing Stages 39 – 41). Events are generated stochastically to meet these criteria, and  
545 are assumed to occur at random times within each of the specified periods. We generate 1,000  
546 such populations, and in Figure 11b we plot the median value of  $\Sigma M_O$  as a function of  $V$ , and

547 the boundaries containing 95% of the models. The resulting models show good agreement  
 548 with the observed evolution of cumulative moment release.

549 This modelling indicates the need for caution when attempting to constrain the relationship  
 550 between moment release and volume: if the constant of proportionality varies during injection  
 551 then a simple comparison of moment and volume may lead to under- or overestimates of the  
 552 exponent  $n$ . For this dataset, a linear relationship between cumulative moment and volume,  
 553 with an increase in  $S_{EFF}$  from  $\log_{10} S_{EFF} = -2.6$  to  $\log_{10} S_{EFF} = -1.7$  during reactivation of the  
 554 NEF-1 fault, provides a good fit to the observed seismicity.

555



556

557 *Figure 11: Evolution of cumulative seismic moment with injection volume. In (a), data points*  
 558 *are coloured by the corresponding stage. Power law fits to the observations are shown, with*  
 559 *a best-fit exponent of  $n = 1.61$  for the overall dataset (dark grey dashed line), but  $n = 0.77$  for*  
 560 *the early stages,  $n = 2.98$  where the NEF-1 reactivates, and  $n = 0.58$  during the final stages*  
 561 *(orange dashed lines). In (b) the red curve shows the observed data, the black line shows the*  
 562 *median stochastically-simulated model as described in Section 5.3, with the shaded region*  
 563 *representing 95% of the models.*

564

#### 565 **5.4. Assigning injection volumes to seismicity**

566 Verdon and Budge (2018) treated each hydraulic fracturing stage as an independent event,  
 567 and did not treat the volumes cumulatively as injection stages proceeded. In contrast, for the  
 568 PNR-1z dataset, Figures 9 and 10 show the importance of treating multiple stages in a  
 569 cumulative manner, and that failure to do so would have produced a significant underestimate  
 570 of the expected event magnitudes for some stages. We believe that the difference in  
 571 behaviours between the two sites stems from the orientations of the faults relative to the well  
 572 trajectories. In the Horn River Basin site described by Verdon and Budge (2018), the  
 573 reactivated faults were orientated roughly perpendicular to the wells. As such, each

574 seismogenic feature was only affected by one or two stages (Kettley *et al.*, 2019). In contrast,  
575 for PNR-1z the NEF-1 fault runs obliquely to the well, and so this feature was intersected by  
576 multiple fracture stages, hence the need to treat these stages cumulatively.

577 Assigning the appropriate fluid volume when making such assessments remains a challenging  
578 issue (e.g., Atkinson *et al.*, 2016). The comparison of the Horn River Basin and PNR-1z  
579 examples described above shows that detailed analysis of microseismic event locations,  
580 combined with a geomechanical understanding of the subsurface, is needed to guide such  
581 decisions.

582

## 583 **6. Conclusions**

584 Recent hydraulic fracturing operations at the Preston New Road PNR-1z well were subject to  
585 some of the most stringent regulations regarding induced seismicity ever applied to any kind  
586 of industrial activity. The operator therefore took a proactive approach to the issue, using real  
587 time microseismic monitoring to make operational decisions with respect to induced  
588 seismicity. Microseismic observations allowed us to identify the presence of a pre-existing  
589 structure on which elevated levels of seismicity was occurring, and to map its extent in the  
590 subsurface. This structure produced multiple events that were above the TLS red light  
591 threshold, forcing the operator to stop injection, resulting in wasted stages, where fluid  
592 injection ceased before significant quantities of proppant could be placed. Using the  
593 microseismic observations, the operator was able to move to injection locations that were less  
594 likely to interact with this structure, thereby increasing the chance of conducting successful  
595 stages.

596 At the same time, we used the microseismic observations to populate a statistical model to  
597 estimate an upper bound for the largest expected event size during injection. This model was  
598 successful in forecasting the magnitudes of the events that did occur. The forecast maximum  
599 magnitudes of  $M_{MAX} < 2$  was within the overall objective set by the regulator to minimise the  
600 number of felt events and eliminate the possibility of damaging events. This modelling gave  
601 the operator and the regulator confidence that, even if the seismogenic structure were to be  
602 intersected by further fracturing stages, the level of risk posed was acceptable. This  
603 confidence was borne out during operations: as further activity did occur on the identified  
604 fault, but the largest event to occur had a magnitude of  $M = 1.5$ , within the expectations  
605 provided by the statistical model.

606 Various options have been suggested to regulate induced seismicity. Fault respect distances  
607 (Westwood *et al.*, 2017) require an operator to avoid known faults in the subsurface.

608 However, this case study, along with previous cases (e.g., Igonin *et al.*, 2019; Kettleby *et al.*,  
609 2019) shows that reactivated faults may not be visible on 3D seismic surveys, especially if  
610 they have strike slip displacement, while imaged faults may not be near to their critical stress  
611 and therefore don't reactivate. Therefore the use of fault respect distances will not provide an  
612 effective approach to induced seismicity regulation.

613 Whereas more advanced approaches to the mitigation of induced seismicity have been  
614 proposed (e.g., Mignan *et al.*, 2017; Verdon and Budge, 2018) and demonstrated (Kwiatek *et*  
615 *al.*, 2019), simple Traffic Light Schemes are the most common form of regulation applied by  
616 regulators to mitigate HF-IS. The retroactive nature of these TLSs means that red light  
617 thresholds may be set far lower than the actual level of seismicity that a regulator wishes to  
618 prevent. Decisions are based solely on the magnitude of the largest events, which is a  
619 reasonable choice if sites are monitored by regional arrays that provide limited detection  
620 thresholds and poorly-constrained event locations. However, where operators acquire high-  
621 quality real-time microseismic data, providing thousands of accurately-located events across  
622 several orders of magnitude, then a TLS that use only the largest event magnitude, and  
623 therefore discards 99.9% of the observations available, seems unnecessarily crude. In this  
624 paper we have demonstrated how an operator can use microseismicity to assess the seismic  
625 risk, and make proactive decisions to mitigate induced seismicity in real time. Such an  
626 approach is more in line with the type of goal-setting regulation (Lindøe *et al.*, 2012) that has  
627 been applied with much success to other aspects of the oil and gas industry. Induced  
628 seismicity poses a risk for other forms of sub-surface industrial activity including engineered  
629 geothermal systems, and the storage of CO<sub>2</sub> in geologic reservoirs. As induced seismicity  
630 continues to attract public scrutiny, the proactive real-time use of seismic monitoring, as  
631 demonstrated here, could see many other applications.

632

### 633 **Data and Resources**

634 The event catalogues and injection data used in this paper are scheduled to be released by the  
635 Oil and Gas Authority (<https://www.ogauthority.co.uk/data-centre/>) on the 27<sup>th</sup> June 2019.

636

### 637 **Acknowledgements**

638 We would like to thank Cuadrilla Resources and their joint venture partners Spirit Energy and  
639 A J Lucas for collaboration on this project. We would like to thank the BGS for providing  
640 data from the additional surface stations that were installed at the site. We would also like to

641 thank Schlumberger for processing the monitoring data in real time. JPV was funded by  
642 NERC Grant NE/R018162/1, TK was supported by the NERC GW4+ Doctoral Training  
643 Partnership (Grant NE/L002434/1), and JMK and AFB were funded by NERC Grant  
644 NE/R018006/1.

645

## 646 **References**

- 647 Aki K., 1965. Maximum likelihood estimate of  $b$  in the formula  $\log N = a - bM$  and its  
648 confidence limits: Bulletin of the Earthquake Research Institute, University of Tokyo 43,  
649 237-239.
- 650 Akkar S., M.A. Sandikkaya, J.J. Bommer, 2014. Empirical ground-motion models for point-  
651 and extended-source crustal earthquake scenarios in Europe and the Middle East: Bulletin  
652 of Earthquake Engineering 12, 359-387.
- 653 Atkinson, G.M., D.W. Eaton, H. Ghofrani, D. Walker, B. Cheadle, R. Schultz, R. Shcherbakov,  
654 K. Tiampo, J. Gu, R.M. Harrington, Y. Liu, M. van der Baan, H. Kao, 2016. Hydraulic  
655 fracturing and seismicity in the Western Canada Sedimentary Basin: Seismological  
656 Research Letters 87, 631-647.
- 657 Baisch S., C. Koch, A. Muntendam-Bos, 2019. Traffic Light Systems: To what extent can  
658 induced seismicity be controlled: Seismological Research Letters, in press.
- 659 Bao X. and D.W. Eaton, 2016. Fault activation by hydraulic fracturing in western Canada:  
660 Science 354, 1406-1409.
- 661 Bosman K., A. Baig, G. Viegas, T. Urbancic, 2016. Towards an improved understanding of  
662 induced seismicity associated with hydraulic fracturing: First Break 34, 61-66.
- 663 Broccardo M., A. Mignan, S. Wiemer, B. Stojadinovic, D. Giardini, 2017. Hierarchical  
664 Bayesian modeling of fluid-induced seismicity: Geophysical Research Letters 44, 11,357-  
665 11,367.
- 666 Butcher A., R. Lockett, J.P. Verdon, J-M. Kendall, B. Baptie, J. Wookey, 2017. Local  
667 magnitude discrepancies for near-event receivers; implications for the UK traffic light  
668 scheme: Bulletin of the Seismological Society of America 107, 532-541.
- 669 Cuadrilla Resources Ltd., 2018. Preston New Road 1z Hydraulic Fracture Plan. Accessed at:  
670 [https://consult.environment-agency.gov.uk/onshore-oil-and-gas/information-on-cuadrillas-](https://consult.environment-agency.gov.uk/onshore-oil-and-gas/information-on-cuadrillas-preston-new-road-site/supporting_documents/Preston%20New%20Road%20HFP.pdf)  
671 [preston-new-road-site/supporting\\_documents/Preston%20New%20Road%20HFP.pdf](https://consult.environment-agency.gov.uk/onshore-oil-and-gas/information-on-cuadrillas-preston-new-road-site/supporting_documents/Preston%20New%20Road%20HFP.pdf) on  
672 25/3/2019.
- 673 Chambers K., J-M. Kendall, S. Brandsberg-Dahl, J. Rueda, 2010. Testing the ability of surface  
674 arrays to monitor microseismic activity: Geophysical Prospecting 58, 821-830.
- 675 Chen X., J. Haffener, T.H.W. Goebel, X. Meng, Z. Peng, J.C. Chang, 2018. Temporal  
676 correlation between seismic moment and injection volume for an induced earthquake  
677 sequence in central Oklahoma: Journal of Geophysical Research 123, 3047-3064.
- 678 Clarke H., L. Eisner, P. Styles, P. Turner, 2014. Felt seismicity associated with shale gas  
679 hydraulic fracturing: The first documented example in Europe: Geophysical Research  
680 Letters 41, 8308-8314.
- 681 Clauset A., C.R. Shalizi, M.E.J. Newman, 2009. Power-law distributions in empirical data:  
682 Society for Industrial and Applied Mathematics Review 51, 661-703.
- 683 De Barros L., F. Cappa, Y. Guglielmi, L. Duboeuf, J-R. Grasso, 2019. Energy of injection-  
684 induced seismicity predicted from *in-situ* experiments: Nature Scientific Reports 9:4999.
- 685 Dinske C. and S. Shapiro, 2013. Seismotectonic state of reservoirs inferred from magnitude  
686 distributions of fluid-induced seismicity: Journal of Seismology 17, 13-25.



687 Edwards B. and J. Douglas, 2014. Magnitude scaling of induced earthquakes: Geothermics  
688 52, 132-139.

689 Eyre T.S., D.W. Eaton, M. Zecevic, D. D'Amico, D. Kolos, 2019. Microseismicity reveals  
690 fault activation before  $M_w$  4.1 hydraulic-fracturing induced earthquake: Geophysical  
691 Journal International 218, 534-546.

692 Fellgett M.W., A. Kingdon, J.D.O. Williams, C.M.A. Gent, 2017. State of stress across UK  
693 regions: British Geological Society, Nottingham, UK. Open File Report OR/17/048.

694 Friberg P.A., G.M. Besana-Ostman, I. Dricker, 2014. Characterisation of an earthquake  
695 sequence triggered by hydraulic fracturing in Harrison County, Ohio: Seismological  
696 Research Letters 85, 1295-1307.

697 Galis M., J.P. Ampuero, P.M. Mai, F. Cappa, 2017. Induced seismicity provides insight into  
698 why earthquake ruptures stop: Science Advances 3, eaap7528.

699 Green C.A., P. Styles, B.J. Baptie, 2012. Preese Hall shale gas fracturing review and  
700 recommendations for induced seismic mitigation. Department of Energy and Climate  
701 Change, London.

702 Grigoli F., S. Cesca, A.P. Rinaldi, A. Manconi, J.A. López-Comino, J.F. Clinton, R.  
703 Westaway, C. Cauzzi, T. Dahm, S. Wiemer, 2018. The November 2017 MW 5.5. Pohang  
704 earthquake: A possible case of induced seismicity in South Korea: Science 360, 1003-  
705 1006.

706 Gutenberg B., and C.F. Richter, 1944. Frequency of earthquakes in California: Bulletin of the  
707 Seismological Society of America 34, 185-188.

708 Hallo M., I. Oprsal, L. Eisner, M.Y. Ali, 2014. Prediction of magnitude of the largest  
709 potentially induced seismic event: Journal of Seismology 18, 421-431.

710 Hammack R., W. Harbert, S. Sharma, B. Stewart, R. Capo, A. Wall, A. Wells, R. Diehl, D.  
711 Blaushild, J. Sams, G. Veloski, 2014. An Evaluation of Fracture Growth and Gas/Fluid  
712 Migration as Horizontal Marcellus Shale Gas Wells are Hydraulically Fractured in Greene  
713 County, Pennsylvania: EPA Technical Report Series, U.S. Department of Energy,  
714 National Energy Technology Laboratory, Pittsburgh, PA, NETL-TRS-3-2014.

715 Hansard, 2018. House of Commons Official Report 649(208), 714-716.

716 Häring M.O., U. Schanz, F. Ladner, B.C. Dyer, 2008. Characterisation of the Basel 1 enhanced  
717 geothermal system: Geothermics 37, 469-495.

718 Hofmann H., G. Zimmermann, A. Zang, K-B. Min, 2018. Cyclic soft stimulation (CSS): A new  
719 fluid injection protocol and traffic light system to mitigate seismic risks of hydraulic  
720 stimulation treatments: Geothermal Energy 6, 27.

721 Hofmann H., G. Zimmermann, M. Farkas, E. Huenges, A. Zang, M. Leonhardt, G. Kwiątek, P.  
722 Martinez-Garzon, M. Bohnhoff, K-B. Min, P. Fokker, R. Westaway, F. Bethmann, P. Meier,  
723 K.S. Yoon, J.W. Choi, T.J. Lee, K.Y. Kim, 2019. First field application of cyclic soft  
724 stimulation at the Pohang enhanced geothermal system site in Korea: Geophysical Journal  
725 International 217, 926-949.

726 Igonin N., J.P. Verdon, J-M. Kendall, D.W. Eaton, 2019. The importance of pre-existing  
727 fracture networks for fault reactivation during hydraulic fracturing: Journal of Geophysical  
728 Research, *sub judice*.

729 Kendall J-M., A. Butcher, A.L. Stork, J.P. Verdon, R. Lockett, B.J. Baptie, 2019. How big is a  
730 small earthquake? Challenges in determining microseismic magnitudes: First Break 37, 51-  
731 56.

732 Keranen K.M., M. Weingarten, G.A. Abers, B.A. Bekins, S. Ge, 2014. Sharp increase in central  
733 Oklahoma seismicity since 2008 induced by massive wastewater injection: Science 345,  
734 448-451.

735 Kettlety T., J.P. Verdon, M.J. Werner, J-M. Kendall, J. Budge, 2019. Investigating the role of  
736 elastostatic stress transfer during hydraulic fracturing-induced fault reactivation:  
737 Geophysical Journal International 217, 1200-1216.

738 Kwiatek G., T. Saamo, T. Ader, F. Bluemle, M. Bohnhoff, M. Chendorain, G. Dresen, P.  
739 Heikkinen, I. Kukkonen, P. Leary, M. Leonhardt, P. Malin, P. Martinez-Garzon, K.  
740 Passmore, P. Passmore, S. Valenzuela, C. Wollin, 2019. Controlling fluid-induced  
741 seismicity during a 6.1-km-deep geothermal stimulation in Finland: *Science Advances* 5,  
742 eaav7224.

743 Li X., I. Main, A. Jupe, 2018. Induced seismicity at the UK ‘hot dry rock’ test site for  
744 geothermal energy production: *Geophysical Journal International* 214, 331-344.

745 Lindøe P.H., M. Baram, J. Paterson, 2012. Robust Offshore Risk Regulation – an assessment  
746 of US, UK and Norwegian approaches: European Safety and Reliability Conference,  
747 Helsinki.

748 Luckett R., L. Ottemoller, A. Butcher, B. Baptie, 2019. Extending local magnitude  $M_L$  to  
749 short distances: *Geophysical Journal International* 216, 1145-1156.

750 Maxwell S.C., J. Shemeta, E. Campbell, D. Quirk, 2008. Microseismic deformation rate  
751 monitoring: SPE Annual Technical Conference, SPE116596.

752 Maxwell S.C., M. Jones, R. Parker, S. Miong, S. Leaney, D. Dorval, D. D’Amico, J. Logel, E.  
753 Anderson, K. Hammermaster, 2009. Fault activation during hydraulic fracturing: SEG  
754 Annual Meeting Expanded Abstracts 28, 1552-1556.

755 Maxwell S.C., J. Rutledge, R. Jones, M. Fehler, 2010. Petroleum reservoir characterization  
756 using downhole microseismic monitoring: *Geophysics* 75, A129-A137.

757 Mignan A., M. Broccardo, S. Wiemer, D. Giardini, 2017. Induced seismicity closed-form  
758 traffic light system for actuarial decision-making during deep fluid injections: *Nature*  
759 *Scientific Reports* 7:13607.

760 Oil and Gas Authority, 2018. Consolidated Onshore Guidance, Version 2.2. Oil and Gas  
761 Authority, London. Accessed at:  
762 [https://www.ogauthority.co.uk/media/4959/29112017\\_consolidated-onshore-guidance-](https://www.ogauthority.co.uk/media/4959/29112017_consolidated-onshore-guidance-compendium_vfinal-002.pdf)  
763 [compendium\\_vfinal-002.pdf](https://www.ogauthority.co.uk/media/4959/29112017_consolidated-onshore-guidance-compendium_vfinal-002.pdf) on 5/04/2019.

764 Schultz R., V. Stern, M. Novakovic, G. Atkinson, Y.J. Gu, 2015. Hydraulic fracturing and the  
765 Crooked Lake sequences: Insights gleaned from regional seismic networks: *Geophysical*  
766 *Research Letters* 42, 2750-2758.

767 Schultz R., G. Atkinson, D.W. Eaton, Y.J. Gu, H. Kao, 2018. Hydraulic fracturing volume is  
768 associated with induced earthquake productivity in the Duvernay play: *Science* 359, 304-  
769 308.

770 Segall, P., 1989. Earthquakes triggered by fluid extraction: *Geology* 17, 942-946.

771 Shapiro S.A., C. Dinske, C. Langenbruch, 2010. Seismogenic index and magnitude  
772 probability of earthquakes induced during reservoir fluid stimulations: *The Leading Edge*  
773 29, 304-309.

774 Skoumal R.J., M.R. Brudzinski, B. S. Currie, 2015. Induced earthquakes during hydraulic  
775 fracturing in Poland Township, Ohio: *Bulletin of the Seismological Society of America*  
776 105, 189-197.

777 van der Elst, N.J., M.T. Page, D.A. Weiser, T.H.W. Goebel, S.M. Hosseini, 2016. Induced  
778 earthquake magnitudes are as large as (statistically) expected: *Journal of Geophysical*  
779 *Research* 121, 4575-4590.

780 Verdon J.P., 2014. Significance for secure CO<sub>2</sub> storage of earthquakes induced by fluid  
781 injection: *Environmental Research Letters* 9, 064022.

782 Verdon J.P. and J. Budge, 2018. Examining the capability of statistical models to mitigate  
783 induced seismicity during hydraulic fracturing of shale gas reservoirs: *Bulletin of the*  
784 *Seismological Society of America* 108, 690-701

785 Wang Z. and A. Krupnick, 2013. A retrospective review of shale gas development in the  
786 United States: What lead to the boom?: *Resources for the Future* DP 13-12.

787 Webster B., 2018. Cuadrilla to resume fracking seven years after tremors: The Times, 16<sup>th</sup>  
788 October 2018. Accessed at: [https://www.thetimes.co.uk/article/cuadrilla-to-resume-](https://www.thetimes.co.uk/article/cuadrilla-to-resume-fracking-seven-years-after-tremors-h6lrdhxj)  
789 [fracking-seven-years-after-tremors-h6lrdhxj](https://www.thetimes.co.uk/article/cuadrilla-to-resume-fracking-seven-years-after-tremors-h6lrdhxj) on 28/3/2019.

790 Wessels, S.A., A. De La Peña, M. Kratz, S. Williams-Stroud, T. Jbeili, 2011. Identifying  
791 faults and fractures in unconventional reservoirs through microseismic monitoring: First  
792 Break 29, 99-104.

793 Westwood R.F., S.M. Toon, P. Styles, N.J. Cassidy, 2017. Horizontal respect distance for  
794 hydraulic fracturing in the vicinity of existing faults in deep geological reservoirs: a  
795 review and modelling study: Geomechanics and Geophysics for Geo-Energy and Geo-  
796 Resources 3, 379-391.

797 Wiemer S. and M. Wyss, 2000. Minimum magnitude of completeness in earthquake catalogs:  
798 Examples from Alaska, the western United States, and Japan: Bulletin of the  
799 Seismological Society of America 90, 859-869.

800 Williams M.J. and J. Le Calvez, 2013. Reconstructing frequency-magnitude statistics from  
801 detection limited microseismic data: Geophysical Prospecting 61, 20-38.

802 Zang A., G. Zimmermann, H. Hofmann, O. Stephansson, K-B. Min, K.Y. Kim, 2019. How to  
803 reduce fluid-injection-induced seismicity: Rock Mechanics and Rock Engineering 52, 475-  
804 493.

805 Zinno R., J. Gibson, R.N. Walker Jr, R.J. Withers, 1998. Overview: Cotton Valley hydraulic  
806 fracture imaging project: SEG Annual Meeting Expanded Abstracts 17, 338-341.

807

808

809

810

811